Large area transparent refractory aerogels with high solar thermal performance

Zachary J. Berquist,[†]
Andrew J. Gayle,[§]
Andrés Miranda Mañón[†]
Victor Vogt[#]
Keyi Kang Yao[◊]
Vishnu Ramasawmy[◊]
Kyle Wilke[◊]
Neil P. Dasgupta,[§#*]
Andrej Lenert[†*]

[†]Department of Chemical Engineering, University of Michigan, Ann Arbor, MI 48109
[§]Department of Mechanical Engineering, University of Michigan, Ann Arbor, MI 48109
[#]Department of Materials Science and Engineering, University of Michigan, Ann Arbor, MI 48109
◊AeroShield Materials, Hyde Park, MA, 02136
*E-mails: ndasgupt@umich.edu; alenert@umich.edu

Abstract

Application of transparent silica aerogels in low-temperature solar thermal systems has led to major improvements in performance. In high temperature concentrating solar thermal (CST) systems, aerogels have yet to demonstrate the necessary scalability, stability, and performance to support their widespread deployment. Here, large-area transparent refractory aerogel tiles are synthesized and shown to achieve a record-high receiver figure-of-merit (FOM) at high temperatures. The work leverages a scaled-up process for sol-gel synthesis to control the density of the aerogels for improved solar transmittance and adapts a previous atomic layer deposition (ALD) technique with the aid of predictive reaction-transport modeling. After aging for 10 days at 700 ºC, the large-area tiles exhibit a solar-weighted transmittance of 95.6% and a thermal emittance of 0.31, corresponding to a figure-of-merit (FOM) of 80% at 100 suns and 700 ºC. The observed sintering rates at 700 ºC are comparably low to earlier one-inch aerogels, suggesting long-term stability under relevant operating conditions. The study indicates that refractory aerogels are scalable materials for efficient photothermal conversion at high temperatures.

Keywords: aerogels, solar thermal, concentrating solar power, solar industrial process heat, atomic layer deposition, selective receiver

1. Introduction

Concentrating solar thermal (CST) is a promising solution to decarbonize industrial process heat and baseload electricity generation. Next-generation CST designs aim to operate at temperatures in excess of 550 °C to enable more efficient supercritical CO_2 (sCO_2) power cycles [1] and meet the demands for high-grade solar industrial process heat (SIPH) [2,3,4,5,6,7,8]. Among various collector technologies, linear concentrating systems such as parabolic trough collectors are appealing due to their high optical efficiencies and low capital costs compared to analogous two-axis concentrating systems such as solar power towers [9,10]. Furthermore, linear systems are modular and capable of supplying outputs as low as ~100 kW_{th}. A primary challenge with linear CST is achieving efficient solar-to-thermal conversion at high temperatures because of the limited solar flux incident on the receiver surface (30-60 kW/m^2), which is of comparable magnitude to the blackbody emissive power of ~50 kW/m^2 at 700 °C. To limit thermal losses, commercial systems use selective absorbers and operate in vacuum, which prevents degradation of the absorber coating and minimizes convective losses. At higher temperatures, however, there is a lack of stable, high performance selective coatings [11,12]. Furthermore, operating under high vacuum adds cost and can lead to shortened lifetimes.

Solar-transparent aerogels have the potential to improve the efficiency and operational stability of CST systems [13,14,15,16,17,18,19,20,21,22,23]. As illustrated in Fig. 1a, aerogels are highly porous, low-thermal conductivity materials that transmit the incident solar flux and insulate the hot absorber surface (or cavity). In addition to minimizing convective and conductive losses, they leverage a greenhouse trapping mechanism to reduce radiative heat losses, which involves absorption and re-emission of thermal radiation at progressively lower temperatures. The aerogel approach offers two distinct advantages compared to vacuum-based selective absorbers. First, aerogels can enable the use of non-selective absorbers such as black paints or blackbody cavities that are more stable at high temperatures and in air [24]. Second, silica aerogels can eliminate the

need for high vacuum, allowing operation of solar receivers at near-ambient pressures or extending the receiver lifetime.

One challenge with silica aerogels is that they sinter at higher temperatures, which typically limits their use to below 600 °C [25,26]. To improve the thermal robustness of aerogels, research efforts have aimed at modifying the solid framework through templating or the addition of secondary phases[23,27,28,29,30,31,32,33,34,35]. Specifically, our previous work introduced a process to conformally modify the interior surfaces of silica aerogels with alumina using a single cycle of atomic layer deposition (ALD) operated in a quasi-static mode (QSM)[31]. Compared to native silica aerogels, the resulting alumina-silica aerogels (named refractory aerogels) exhibited similarly high solar transmittance and improved high temperature stability up to 800 °C[23].

Another important challenge with aerogels is maintaining the optical and thermal properties of aerogels at sufficiently large scales for integration in CST systems. Prior studies using refractory aerogels have been limited to aerogels measuring one-inch in diameter, which is too small for application in utility-scale CST. Each absorber tube segment in a linear CST plant is typically 4 m long and 70 mm in diameter [36]. To cover the solar-incident area of the absorber tube with aerogel segments, the characteristic length scale of the aerogel tiles should be at least 10 cm. The main challenge when producing larger silica aerogel tiles is that they are highly brittle materials. As the size increases, brittle fracture occurs more easily because for a given body force, the resulting maximum bending moment will be higher for a larger sample. Larger aerogels therefore become increasingly difficult to handle during processing, which requires the design of special molds and racks to successfully create and transport crack-free tiles within the dimensional tolerance. Efforts to improve the fracture strength of silica aerogels have resulted in reduced transmittance/clarity or increased thermal conductivity [32,35,37,38,39,40,41]. Furthermore, applying ALD at these scales can also be challenging due to the high surface areas and the effectively ultra-high aspect ratios of

the pores that are inherent to the materials. This can lead to substantial ALD precursor waste and long process times, adding significant expense to the manufacturing process [42].

Here, we demonstrate large-area refractory aerogel tiles that are stable at high temperatures and achieve a record-high solar thermal figure-of-merit (FOM). In doing so, the work establishes de-risked processing techniques for both the aerogel synthesis and subsequent ALD modification. Various aerogel densities are explored to optimize solar thermal performance. Optical and thermal characterization indicates that the refractory aerogel tiles exhibit higher solar transmittance combined with similar thermal emittance and long-term stability as the benchmark one-inch aerogels. Given their scale, stability, and solar thermal performance, the aerogel tiles shown here have potential for widespread application in high temperature solar thermal systems.

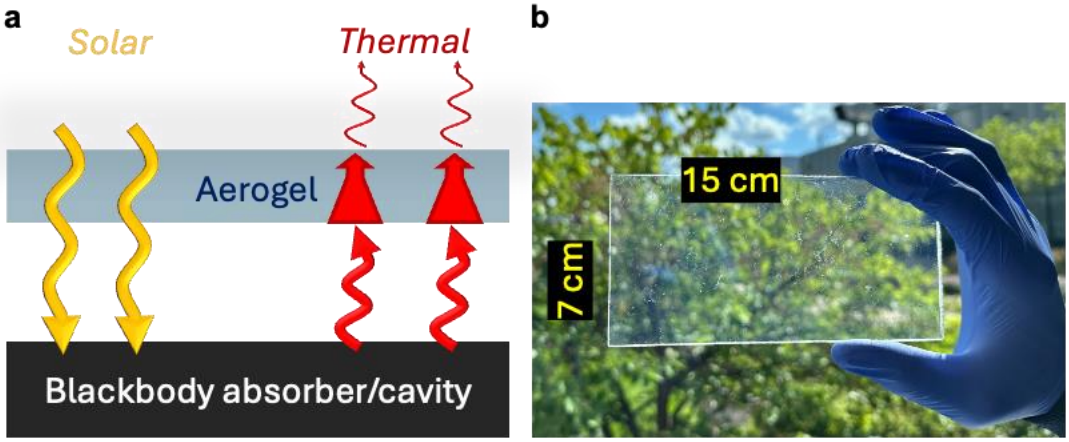

Figure 1. Mechanism of solar heat trapping using transparent aerogels and large area tiles for concentrating solar thermal (CST) applications. (a) Transparent aerogels transmit sunlight to heat a black absorber (or blackbody cavity) and limit thermal losses out of the receiver. (b) Image of a transparent aerogel tile used in this study, measuring 7 cm by 15 cm.

2. Aerogel fabrication

Two densities of aerogel tiles are prepared and investigated in this study. The initial densities (prior to ALD) of the low density (LD) and medium density (MD) aerogels are 65 and 140 kg/m^3, respectively. The relevant properties of these aerogels are compared against our earlier benchmark high density (HD) refractory aerogels which had an initial density of 160 kg/m^3. All three aerogels (LD, MD, HD) use the same synthesis chemistry but the ratios of the four reagents (tetramethylorthosilicate, concentrated ammonia, deionized water, and methanol) in the gelation stage are controlled to tune the density and optimize transmittance. By increasing the relative concentration of the silica precursor to the other reagents, the bulk and skeletal density of the material increases. Subsequent critical point drying and annealing results in shrinkage of the tiles, which leads to additional bulk density increase [26,43,44]. Large aerogel sheets (13 x 19 inch) are first synthesized using a proprietary process developed at AeroShield Materials based on aerogel manufacturing processes tailored to produce high-transparency sheets [26,44]. This process leverages a 500-liter critical point drying (CPD) system. The aerogels, immersed in methanol, are placed into the CPD at room temperature and pressure. The system is pressurized to 1500 psi with CO_2 over 3 h while maintaining room temperature. After pressurization, methanol is purged from the system and replaced with CO_2 continuously while raising the temperature to 50 °C. The CO_2 exchange process continues until the methanol content in the CPD is reduced to below 0.5%. Lastly, the system is depressurized at 50 °C over a period of 5 h. An extended description of the working mechanism of the CPD system is provided in Supplementary Note #1. These sheets are laser cut into aerogel tiles measuring 7 x 15 cm, as shown in Fig. 1b, which are suitable dimensions for integration into a standard 70-mm parabolic trough receiver.

To stabilize the aerogels at high temperatures, we adapt our previously developed QSM-ALD process [42] which introduces an alumina-based coating. Leveraging QSM-ALD, the surface of aerogel tiles is modified using a single cycle of ALD. Varying the precursor exposure time during

the modification process enables improved tunability of throughput and raw material (ALD precursor) use [42]. Unlike previous techniques to thermally stabilize aerogels, such as mixing refractory oxide precursors during gelation [32,33,34] or during supercritical drying [35], QSM-ALD minimally decreased solar transmittance in the benchmark HD aerogel. This is a consequence of the conformal, uniform nature of the ALD surface modification and the formation of a transparent aluminum silicate phase.

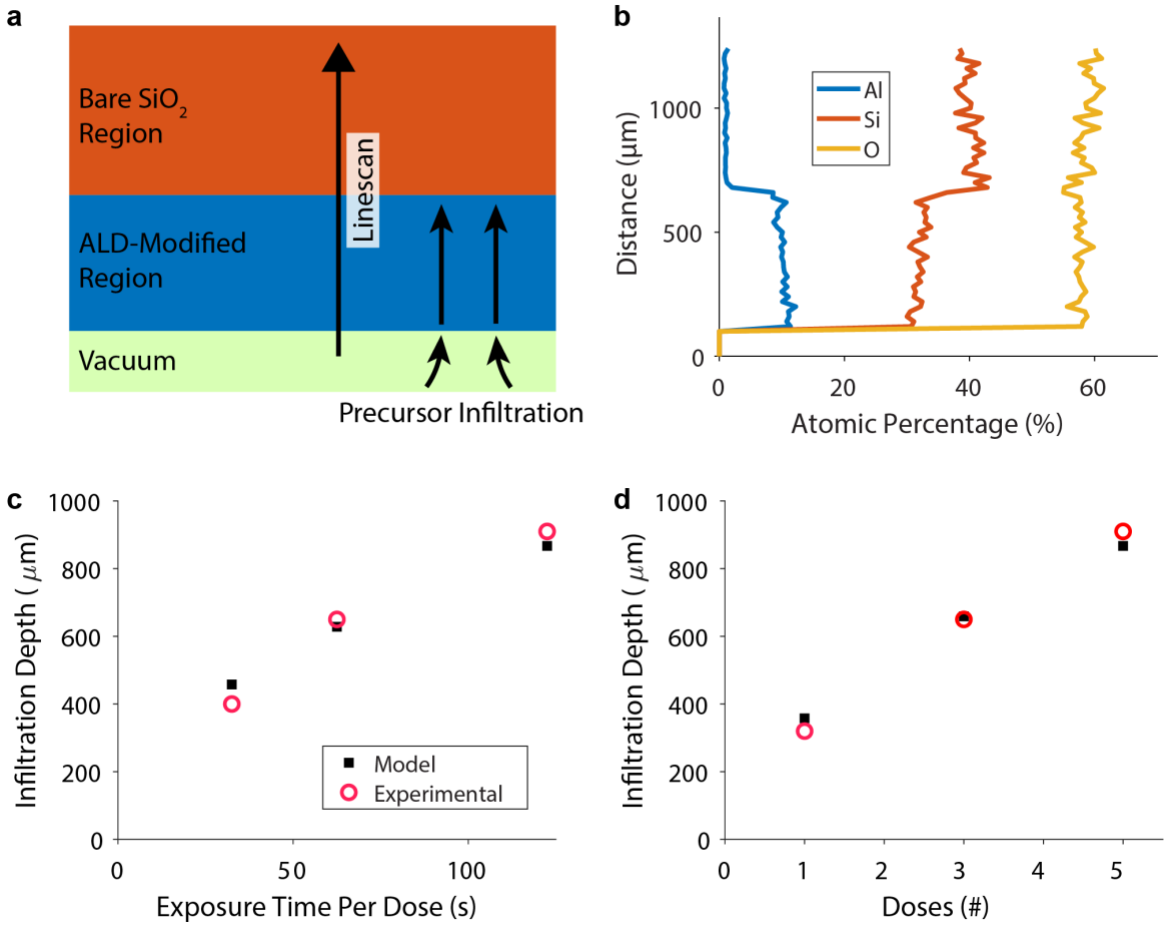

Figure 2. ALD infiltration depth of partially modified aerogels as a function of various process parameters. (a) Schematic showing the cross-section of a partially modified aerogel. The location of the linescan and precursor infiltration direction is shown. (b) EDS linescan showing the percentage of Al, Si, and O through the aerogel cross-section. (c) Variation in exposure time per dose while keeping the number of doses constant, and (d) variation in number of doses while keeping exposure time constant. The experimental infiltration depths for (c) and (d) are for MD aerogels and were measured using optical microscopy (details in Supplementary Note #4). The parameters used for modeling are shown in Supplementary Note #2.

To predict the required conditions for conformal modification of the aerogel tiles, we first calibrate our QSM-ALD process model (further details on the model can be found in Ref. [42]) using small (~12 x 12 x 4 mm) LD and MD samples. In addition to working with lower density aerogels compared to the previous HD samples, we also moved the ALD process to a reactor with a chamber volume 4.5 times larger to allow sufficient room for the larger aerogels tiles to be placed in the ALD chamber [42]. The model is calibrated by varying the exposure time per dose and the number of doses before dosing the counter reactant. The exposure time represents the time that the ALD chamber is isolated from the downstream vacuum pump and upstream gas flows, following dosing of the precursor. By measuring the infiltration depth (Fig. 2) with respect to these two parameters and considering the pore size and specific surface area (see Experimental Section for details), the model is calibrated to these experimental data using the tortuosity as a fitting parameter [42].

The infiltration depth is evaluated using cross-sectional scanning electron microscopy/energy-dispersive X-ray spectroscopy (SEM/EDS) and/or nondestructively using optical microscopy (see Experimental Section and Supplementary Note #4 for details). For model calibration, small LD samples were analyzed via SEM/EDS (Supplementary Note #5), while MD samples were analyzed via optical microscopy (Fig. 2c,d). In the EDS line-scans, the distance of the approximately constant Al signal intensity away from the aerogel surface corresponds to the infiltration depth of the ALD modification (Fig. 2b). Within each SEM/EDS linescan for LD aerogels, the atomic percentage (at%) of Al for each data point deviated from the mean value by approximately ±2.5 at% at most. This uniformity demonstrates that despite the high aspect ratios of aerogels, the self-limiting nature of the ALD reaction is reasonably well maintained [42]. Fig. 2c and 2d show that the modeled and experimental data (in this case collected via optical microscopy) for the MD samples agree (results for the LD samples are shown in Supplementary

Notes #2 and #5). The general trends are captured by the model in the case of both the LD and MD aerogel types, demonstrating that the QSM-ALD model can be applied to lower density aerogels in addition to the benchmark HD aerogels.

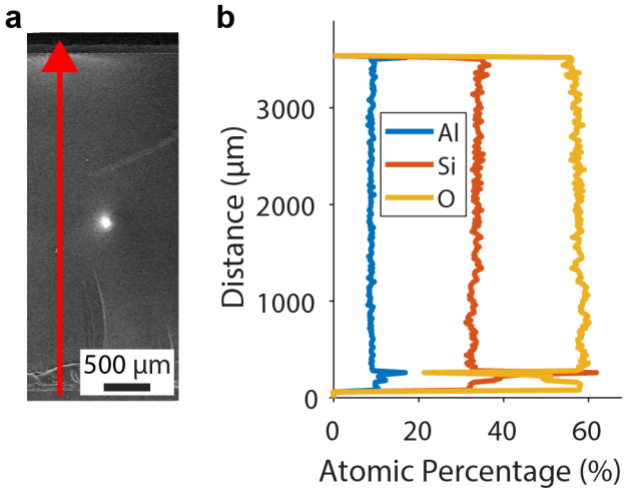

Figure 3. Uniform ALD modification of aerogel tiles. (a) SEM image of the cross-section of a large MD aerogel tile that was conformally modified using a single ALD cycle. The red arrow shows the location of the EDS linescan in (b). (b) EDS linescan showing the percentage of Al, Si, and O through the aerogel cross-section. The noise near the bottom of the cross-section is an artifact of the uneven fracture surface at that location.

We use the calibrated process model to identify the process conditions for QSM-ALD on the aerogel tiles (which are larger by a factor of ~30 in volume compared to benchmark HD aerogels) for complete modification with moderate throughput and raw material usage (see Supplementary Note #6). To this end, we implemented a strategy of varying the exposure time per dose with respect to dose number [42] to help mitigate precursor waste (1% for LD samples and 7% for MD samples) and excessively long process times (12 h for LD samples and 23 h for MD samples). This strategy allows for high levels of precursor utilization compared to using static, short exposure times, while minimizing the increase in process time associated with static, long exposure times (comparisons are shown in Supplementary Note #6). We note that these modifications were performed using lab-scale instruments; on an industrial scale the process times will be significantly shorter.

Fig. 3 shows an example linescan of an aerogel tile following ALD modification. Despite the large size of the tiles, the infiltration is both complete and uniform through the high aspect ratio (up to ~78000:1) of the tiles, as supported by the Al signal (Fig. 3b). The uniform modification of silica aerogel tiles with such high aspect ratios would be difficult or impossible to achieve using traditional line-of-sight techniques such as sputtering or evaporation. The ability to maintain complete, uniform ALD modification on significantly larger substrates is a promising result for further scale-up of refractory aerogel synthesis using the QSM-ALD process.

3. Solar Thermal Performance and Stability

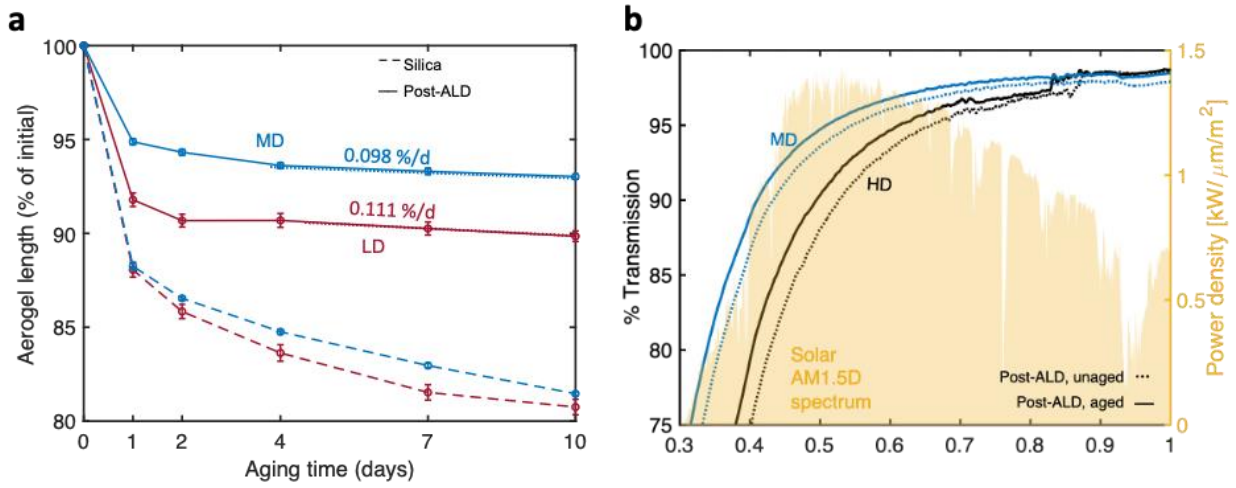

Figure 4. Changes in macroscopic aerogel dimensions and solar transmittance due to aging at 700°C in air. (a) Change in the length of aerogel tiles at 700°C (in air) for the low density (LD) and medium density (MD) aerogels with an ALD coating (solid) and without (dashed). Coated LD and MD tiles exhibit comparably low shrinkage rates to those of the benchmark high-density (HD) aerogels (see also Table 1). Note, ALD itself has a negligible effect on the macroscopic dimensions of the aerogel such as length. (b) The hemispherical transmittance of the coated MD and HD aerogels is high and improves after 700°C aging. Data obtained using a UV-Vis with an integrating sphere. The AM1.5D spectrum is shown for reference.

The performance and stability of the large-area aerogel tiles are evaluated by measuring the aerogel dimensions, mass, optical transmittance, and thermal resistance before and after heat treatment at 700 °C in air. Fig. 4a shows the change in the length of the aerogel tiles at 700 °C.

Without the ALD modification step, the length of the aerogels decreases by almost 20 % upon aging for 10 days at 700 °C. In contrast, the lengths of the LD and MD refractory aerogels (coated with ALD) decrease by 10.2 % and 7.0 % upon aging, respectively, and approach a linear shrinkage rate of 0.111 ± 0.021 %/day and 0.098 ± 0.003 %/day. These results indicate that the ALD treatment improves the high temperature stability of both the LD and MD aerogels. Furthermore, the shrinkage rates of the LD and MD aerogels are comparable to that of the HD benchmark (0.085 ± 0.025%/day). Longer experiments are needed to assess the feasibility and lifetime of this material in practical applications. Lastly, we note that the chemical changes imparted by ALD process help preserve the morphological characteristics of the aerogels after high temperature annealing, which is critical to their optical and thermal performance. Our previous study demonstrated that refractory aerogels maintain a larger specific surface and similar solar transmittance compared to pure silica aerogels after high-temperature aging [46]. Higher porosity is correlated with larger surface areas and smaller particle sizes, which are desirable for suppression of non-radiative heat losses and improved optical clarity. More details about these changes can be found in Supplementary Note #7.

Fig. 4b shows the hemispherical solar transmittance of the aerogel tiles. Following ALD and 700 ºC aging, the coated LD and MD aerogels exhibit solar transmittances of 95.7 % and 95.6 %, respectively, which is higher than the benchmark HD aerogel (94 %). This result demonstrates that high solar transmittance can be achieved at relevant scales for CST using the processes described in the previous section. The transmittance decreases by 2-3 % after the ALD treatment but partially recovers after aging at 700 ºC as shown in the Fig. 4b. This recovery effect in refractory aerogels is analogous to the favorable restructuring identified by Strobach *et al.* when silica aerogels are annealed at lower temperatures [44]. Complete UV-Vis-NIR and FTIR spectral curves before and after heat treatment of refractory and silica aerogels are provided in Supplementary Note #10.

To assess the high-temperature thermal resistance of the large-area aerogels, we used a previously reported technique [22,23] to directly measure heat loss under application-relevant, high-temperature conditions. Specifically, the aerogel is placed between two high-emissivity surfaces maintained at 700 °C and 25-35 °C while the heat losses are measured using calorimetry. The apparent thermal emittance (ε_{app}) is calculated by dividing the measured heat losses by the blackbody emissive power at 700 °C. Table 1 shows that the emittance decreases from 0.36 to 0.31 to 0.30 as the density increases from low (LD) to medium (MD) to high density (HD). These results indicate that the large-area tiles can maintain comparable intrinsic thermal resistance to the benchmark aerogels. The density-dependent trend is observed because higher density aerogels (of the same thickness) have larger infrared absorption coefficients and are thus more insulating to thermal radiation, which is a dominant mode of heat transfer at higher temperatures. In this regime, the optical path length of thermal photons is proportional to the product of density and thickness.

Table 1. Summary of properties of the three aged refractory aerogels. The figure of merit (FOM) is a measure of the thermal efficiency of the receiver (see Equation (1)).

Property	**Units**	**Low density (LD)**	**Medium density (MD)**	**High density (HD)**
Initial density, silica	kg/m^3	65 ± 2	140 ± 1	160 ± 2
Post-ALD density	kg/m^3	81 ± 2	175 ± 2	231 ± 3
Aged density	kg/m^3	111 ± 4	216 ± 2	333 ± 9
Linear shrinkage rate	%/day	0.111 ± 0.02	0.098 ± 0.01	0.085 ± 0.02
Solar transmittance	%	95.7 ± 1.1	95.6 ± 1.0	94.0 ± 1.0
Apparent emissivity (700°C)	-	0.36 ± 0.01	0.31 ± 0.01	0.30 ± 0.01
FOM (700°C, 50 suns)	%	60 ± 1	65 ± 1	64 ± 1
FOM (700°C, 100 suns)	%	78 ± 1	80 ± 1	79 ± 1

To evaluate the measured properties in the context of CST, we used the figure of merit (FOM) for a solar receiver, η, given by:

$$\eta = \tau_{aerogel}\alpha_{abs} - \frac{\varepsilon_{app}\sigma T^4}{H_s} \quad (1)$$

where $\tau_{aerogel}$ is the solar-weighted transmittance of the aerogel, α_{abs} is the solar absorptance of the absorber, σ is the Stefan-Boltzmann constant, T is the temperature of the absorber, H_s is the solar irradiance incident on the receiver (AM 1.5D). This framework allows for a direct comparison of aerogels with selective surface absorbers. $\tau_{aerogel}$ is assumed to be unity in the analysis of selective absorbers since aerogels are not used in conjunction. For aerogel-based receivers, we assume $\alpha_{abs} = 1$ since there are a variety of broadband absorbers or blackbody cavities which have near-unity absorptance throughout the solar spectrum [47,48,49].

Fig. 5 summarizes the solar thermal performance of the aerogels investigated here. Selective absorbers whose emittances are characterized at >700 °C are also included for comparison. The horizontal axis is the thermal resistance which is given by $1 - \varepsilon_{app}$. The y-axis shows the first term in Equation (1) ($\tau_{aerogel}\alpha_{abs}$) which represents the fraction of the solar flux incident on the receiver that is absorbed. In terms of receiver efficiency, higher solar absorption and higher thermal resistance are desired (towards the upper right corner). We note that there are limited examples of materials measured at such high temperatures. Most experimental measurements of absorber emissivity are performed near room temperature which underestimates their high-temperature emittance. For this reason, we restrict our summary to materials that have been measured at temperatures 700 °C or above.

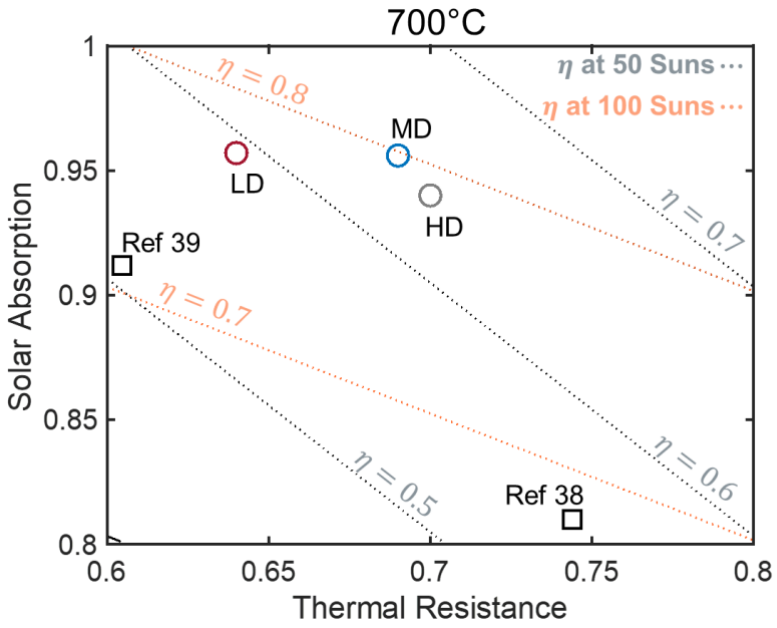

Figure 5. Solar thermal figure-of-merit comparing selective absorbers (squares) and aged refractory aerogels (circles).[50], [51] Only materials that have been experimentally evaluated at temperatures at least 700 °C are shown. Efficiency contour plot at 700 °C and 50 & 100 Suns. We note that the slope of the efficiency contours are a function of irradiance and absorber temperature (see SI note 7).

Fig. 5 presents a contour plot showing η at T = 700 °C and H_s = 50 Suns. These irradiance conditions are representative of parabolic troughs once optical focusing losses and non-ideal irradiance conditions are considered. At these moderate irradiance conditions, the highest performing materials are the refractory aerogel tiles developed here. Not only are they the highest performing, but the aerogels in this study have undergone some of the most extensive thermal aging processes (240 h at 700 °C in air). The medium density (MD) refractory aerogel has the best combination of transparency and thermal resistance resulting in η = 65 % at 700 °C and 50 Suns. If we assume an irradiance range of 75-100 Suns, which could be achieved with very large aperture troughs operating at peak irradiance (1000 W/m^2 direct normal incidence), η at 700 °C increases to 73-80 %. Table 1 summarizes these FOMs alongside measured stability, optical, and thermal properties.

Beyond the aerogel performance and scale demonstrated here, improvements in thermal resistance can further increase the efficiency of aerogel-based receivers. One promising approach is to incorporate transparent conducting oxide (TCO) nanoparticles (NPs) into the aerogel framework to selectively suppress thermal radiation [52]. This technique has the potential to increase thermal resistance to ~0.85. Furthermore, integration and testing in industry relevant receivers is an important next step toward implementation of transparent refractory aerogels in CST.

4. Conclusions

This work demonstrated the feasibility of fabricating large-area refractory aerogels with high-temperature stability and high solar thermal performance at a relevant scale (7 x 15 cm) for application in CST systems. Through calibration measurements using a larger reactor (than in our previous work), our previously reported ALD process model is shown to agree with experimentally measured infiltration depths in aerogel pieces with varying densities. Larger aerogels tiles are modified using a variable exposure time technique to enable the tuning of total process time and raw material use. The resulting 700 °C-aged refractory tiles exhibit high-temperature stability consistent with earlier small-scale benchmark samples. An intermediate initial density of 140 kg/m^3 is shown to optimize solar thermal performance, resulting in a receiver figure-of-merit of 80 % at 700 °C and under 100 Suns irradiance, a record high at such conditions. The outcomes of this work indicate that refractory aerogels can achieve high solar thermal performance at relevant scales and conditions for implementation in CST applications.

5. Experimental Section

5.1 Atomic Layer Deposition

ALD modification of aerogels was performed using a custom-built, cross-flow ALD reactor (chamber volume: ~1200 cm^3) [42]. Trimethylaluminum (TMA, min. 97%, Sigma-Aldrich) and deionized (DI) water were used as precursors. In all cases, a single ALD cycle was performed. The reactor temperature was fixed at 150 °C, and the precursor cylinders were kept at room temperature. The pneumatic valve actuation time of 2.5 s and 1.5 s for TMA and DI water, respectively. Purging was performed using ultra-high-purity Ar (99.999%). Prior to the ALD process for industrial-scale aerogels, the AMs were held under vacuum in the ALD chamber for at least 2 h at 150 °C under constant Ar purging at 70 sccm to remove excess water and other adsorbed species. For small aerogel pieces for calibrating the ALD model, 1 h was used instead. This was followed by 50 DI water doses using an exposure time of 30 s and a purge time of 60 s to ensure hydroxyl termination. For small aerogel pieces, 5 DI water doses were used instead. An additional 300 s purge time was used after the last DI water dose prior to the first TMA dose. During deposition, an equal number of TMA and DI water doses were used.

A multidose-QSM-ALD strategy was used for modifying the aerogel tiles (details in Supplementary Notes #2 and #6). Details for this method can be found in our previous publication [42]. For modifying industrial-scale aerogel tiles, the exposure time was varied from 30 s to 120 s with respect to dose number (Supplementary Note #6). In all cases, purging between doses was performed using Ar with a flow rate of 70 sccm for twice the duration of the exposure time. Details about precursor pulsing, temperature control in the reaction chamber, and precursor partial pressure/ALD growth uniformity can be found in Supplementary Note #6.

5.2 Infiltration Depth Measurements

SEM/EDS linescans were collected using a TESCAN MIRA3 FEG SEM. Measurements were collected along a cross-section through the center of each aerogel, which was made by creating a fracture surface using a razor blade. Optical microscopy (Keyence VHX-7000 4k) was

used in some cases to nondestructively evaluate the infiltration depth, by measuring the distance from the edge of the aerogel to the location of the change of optical contrast. SEM/EDS and optical microscopy average infiltration depth measurements were evaluated for the same sample and found to be similar (within ~20 μm, see Supplementary Note #4).

3636

5.3 Experimental heat loss measurements

The large 7 cm x 15 cm aerogel tiles are cut down further to ~1-inch squares that fit within our thermal heat loss testing setup. The aerogels are placed on a high-emissivity hot stage in a vacuum environment. A commercially available heat flux sensor is covered with blackbody tape to ensure all radiative contributions are collected. The heat flux is then measured at steady state while the hot stage is at 700 °C.

Acknowledgements

This material is based on work by the U.S. Department of Energy's Office of Energy Efficiency and Renewable Energy (EERE) under the Solar Energy Technologies Office (SETO) Award Numbers EE0008526, EE0009376, and EE0009805. The views expressed herein do not necessarily express the view of the U.S. Department of Energy or the United States Government. This work is partially supported by the National Science Foundation under Grant Nos. 2131709 and 1751590. Z.J.B., A.J.G. and V.V. acknowledge support from the National Science Foundation Graduate Student Research Fellowship Program under Grant No. DGE-1256260. Z.J.B. also acknowledge support from the University of Michigan Dow Sustainability Doctoral Research Fellowship and the Mistletoe Research Fellowship. The SEM/EDS work was performed at the Michigan Center for Materials Characterization, which is supported by the College of Engineering at the University of Michigan. The authors acknowledge Alexander J. Hill for contributions on N_2 sorption measurements and analysis.

Conflict of Interest

The authors have the following competing financial interest(s): The authors have filed a patent application related to this work.

References

[1] C. S. Turchi, Z. Ma, T. W. Neises, and M. J. Wagner, "Thermodynamic study of advanced supercritical carbon dioxide power cycles for concentrating solar power systems," *J Sol Energy Eng*, vol. 135, no. 4, pp. 1–7, 2013.

[2] M. Mehos *et al.*, "Concentrating Solar Power Gen3 Demonstration Roadmap," *Nrel/Tp-5500-67464*, no. January, pp. 1–140, 2017, [Online]. Available: https://www.nrel.gov/docs/fy17osti/67464.pdf%0Ahttp://www.nrel.gov/docs/fy17osti/67464.pdf

[3] H. R. Seyf and A. Henry, "Thermophotovoltaics: A potential pathway to high efficiency concentrated solar power," *Energy Environ Sci*, vol. 9, no. 8, pp. 2654–2665, 2016.

[4] N. S. Lewis, "Research opportunities to advance solar energy utilization," *Science (1979)*, vol. 351, no. 6271, 2016.

[5] A. S. Lavine *et al.*, "Thermochemical Energy Storage with Ammonia: Aiming for the SunShot Cost Target," in *AIP Conference Proceedings*, 2016, p. 050028.

[6] G. P. Thiel and A. K. Stark, "To decarbonize industry, we must decarbonize heat," *Joule*, no. 2020, pp. 1–20, 2021.

[7] US Department of Energy, "Solar Research Spotlight: Concentrating Solar- Thermal Power," *Office of Energy Efficiency & Renewable Energy*, 2018, [Online]. Available: https://www.energy.gov/sites/prod/files/2018/09/f55/Concentrating-Solar-Thermal-Power-FactSheet.pdf

[8] Y. L. He, W. Wang, R. Jiang, M. Li, and W. Tao, "Liquid-based high-temperature receiver technologies for next-generation concentrating solar power: A review of challenges and potential solutions," *Frontiers in Energy 2023 17:1*, vol. 17, no. 1, pp. 16–42, Feb. 2023, doi: 10.1007/S11708-023-0866-8.

[9] P. D. Tagle-Salazar, K. D. P. Nigam, and C. I. Rivera-Solorio, "Parabolic trough solar collectors: A general overview of technology, industrial applications, energy market, modeling, and standards," *Green Processing and Synthesis*, vol. 9, no. 1, pp. 595–649, 2020.

[10] N. Kincaid, G. Mungas, N. Kramer, M. Wagner, and G. Zhu, "An optical performance comparison of three concentrating solar power collector designs in linear Fresnel, parabolic trough, and central receiver," *Appl Energy*, vol. 231, no. June, pp. 1109–1121, 2018.

[11] K. Zhang, L. Hao, M. Du, J. Mi, J. Wang, and J. Meng, "A review on thermal stability and high temperature induced ageing mechanisms of solar absorber coatings," *Renewable and Sustainable Energy Reviews*, vol. 67, pp. 1282–1299, 2017.

[12] K. Xu, M. Du, L. Hao, J. Mi, Q. Yu, and S. Li, "A review of high-temperature selective absorbing coatings for solar thermal applications," *Journal of Materiomics*, vol. 6, no. 1, pp. 167–182, 2020.

[13] L. Zhao *et al.*, "Harnessing Heat beyond 200 °C from Unconcentrated Sunlight with Nonevacuated Transparent Aerogels," *ACS Nano*, 2019.

[14] L. Zhao *et al.*, "A Passive High-Temperature High-Pressure Solar Steam Generator for Medical Sterilization," *Joule*, vol. 4, no. 12, pp. 2733–2745, 2020.

[15] A. A. Günay *et al.*, "Optically Transparent Thermally Insulating Silica Aerogels for Solar Thermal Insulation," *ACS Appl Mater Interfaces*, vol. 10, no. 15, pp. 12603–12611, 2018.

[16] K. McEnaney, L. Weinstein, D. Kraemer, H. Ghasemi, and G. Chen, "Aerogel-based solar thermal receivers," *Nano Energy*, vol. 40, no. July, pp. 180–186, 2017.

[17] T. Wang, Q. Si, Y. Hu, G. Tang, and K. J. Chua, "Silica aerogel composited with both plasmonic nanoparticles and opacifiers for high-efficiency photo-thermal harvest," *Energy*, vol. 265, p. 126371, Feb. 2023, doi: 10.1016/J.ENERGY.2022.126371.

[18] D. Gao, L. Wu, Y. Hao, and G. Pei, "Ultrahigh-efficiency solar energy harvesting via a non-concentrating evacuated aerogel flat-plate solar collector," *Renew Energy*, vol. 196, pp. 1455–1468, Aug. 2022, doi: 10.1016/J.RENENE.2022.07.091.

[19] X. Li, R. Li, H. Chang, L. Zeng, Z. Xi, and Y. Li, "Numerical simulation of a cavity receiver enhanced with transparent aerogel for parabolic dish solar power generation," *Energy*, vol. 246, p. 123358, May 2022, doi: 10.1016/J.ENERGY.2022.123358.

[20] L. A. Weinstein *et al.*, "A Hybrid Electric and Thermal Solar Receiver," *Joule*, vol. 2, no. 5, pp. 962–975, 2018, doi: 10.1016/j.joule.2018.02.009.

[21] L. A. Weinstein, J. Loomis, B. Bhatia, D. M. Bierman, E. N. Wang, and G. Chen, "Concentrating Solar Power," *Chem Rev*, vol. 115, no. 23, pp. 12797–12838, Dec. 2015, doi: 10.1021/acs.chemrev.5b00397.

[22] Z. J. Berquist, K. K. Turaczy, and A. Lenert, "Plasmon-enhanced greenhouse selectivity for high-temperature solar thermal energy conversion," *ACS Nano*, vol. 14, no. 10, pp. 12605–12613, Oct. 2020, doi: 10.1021/ACSNANO.0C04982/ASSET/IMAGES/LARGE/NN0C04982_0004.JPEG.

[23] Z. J. Berquist *et al.*, "Transparent Refractory Aerogels for Efficient Spectral Control in High-Temperature Solar Power Generation," *Adv Funct Mater*, vol. 32, no. 12, p. 2108774, Mar. 2022, doi: 10.1002/ADFM.202108774.

[24] C. K. Ho, A. R. Mahoney, A. Ambrosini, M. Bencomo, A. Hall, and T. N. Lambert, "Characterization of Pyromark 2500 Paint for High-Temperature Solar Receivers," *J Sol Energy Eng*, vol. 136, no. 1, pp. 1–4, 2014, doi: 10.1115/1.4024031.

[25] A. Emmerling, W. Lenhard, J. Fricke, and G. A. L. Van De Vorst, "Densification Behaviour of Silica Aerogels upon Isothermal Sintering," *J Solgel Sci Technol*, vol. 8, pp. 837–842, 1997.

[26] E. Strobach, B. Bhatia, S. Yang, L. Zhao, and E. N. Wang, "High temperature stability of transparent silica aerogels for solar thermal applications," *APL Mater*, 2019, doi: 10.1063/1.5109433.

[27] S. Yang, E. Strobach, D. Bierman, L. Zhao, B. Bhatia, and E. N. Wang, "Effect of Al2O3 ALD coating on thermal stability of silica aerogel," *Journal of Porous Materials*, vol. 29, no. 1, pp. 193–200, Feb. 2022, doi: 10.1007/S10934-021-01155-4/FIGURES/4.

[28] X. Yu, X. Ren, X. Wang, G. H. Tang, and M. Du, "A high thermal stability core–shell aerogel structure for high-temperature solar thermal conversion," *Composites Communications*, vol. 37, p. 101440, Jan. 2023, doi: 10.1016/J.COCO.2022.101440.

[29] X. Xu *et al.*, “Double-negative-index ceramic aerogels for thermal superinsulation,” *Science (1979)*, vol. 363, no. 6428, pp. 723–727, Feb. 2019, doi: 10.1126/SCIENCE.AAV7304/SUPPL_FILE/AAV7304S4.MP4.

[30] F. Xiong *et al.*, “Thermal shock protection with scalable heat-absorbing aerogels,” *Nature Communications 2024 15:1*, vol. 15, no. 1, pp. 1–11, Aug. 2024, doi: 10.1038/s41467-024-51530-3.

[31] A. J. Gayle *et al.*, “Tunable Atomic Layer Deposition into Ultra-High-Aspect-Ratio (>60000:1) Aerogel Monoliths Enabled by Transport Modeling,” *Chemistry of Materials*, vol. 33, no. 14, pp. 5572–5583, Jul. 2021, doi: 10.1021/acs.chemmater.1c00770.

[32] R. Saliger, T. Heinrich, T. Gleissner, and J. Fricke, “Sintering behaviour of alumina-modified silica aerogels,” *J Non Cryst Solids*, vol. 186, pp. 113–117, 1995.

[33] P. R. Aravind, P. Mukundan, P. Krishna Pillai, and K. G. K. Warrier, “Mesoporous silica-alumina aerogels with high thermal pore stability through hybrid sol-gel route followed by subcritical drying,” *Microporous and Mesoporous Materials*, vol. 96, no. 1–3, pp. 14–20, 2006.

[34] H. Tamon, T. Sone, M. Mikami, and M. Okazaki, “Preparation and Characterization of Silica – Titania and Silica – Alumina Aerogels,” *J Colloid Interface Sci*, no. 188, pp. 493–500, 1997.

[35] G. Zu *et al.*, “Highly thermally stable zirconia/silica composite aerogels prepared by supercritical deposition,” *Microporous and Mesoporous Materials*, vol. 238, pp. 90–96, 2017, doi: 10.1016/j.micromeso.2016.03.005.

[36] F. Burkholder and C. Kutscher, “Heat Loss Testing of Schott’s 2008 PTR70 Parabolic Trough Receiver,” no. May, 2009.

[37] N. Leventis, C. Sotiriou-Leventis, G. Zhang, and A. M. M. Rawashdeh, “Nanoengineering Strong Silica Aerogels,” *Nano Lett*, vol. 2, no. 9, pp. 957–960, 2002, doi: 10.1021/nl025690e.

[38] B. Himmel, T. Gerber, H. Bürger, G. Holzhüter, and A. Olbertz, “Structural characterization of SiO2-Al2O3 aerogels,” *J Non Cryst Solids*, vol. 186, pp. 149–158, 1995.

[39] J. C. H. Wong, H. Kaymak, S. Brunner, and M. M. Koebel, “Mechanical properties of monolithic silica aerogels made from polyethoxydisiloxanes,” *Microporous and Mesoporous Materials*, vol. 183, pp. 23–29, 2014, [Online]. Available: http://dx.doi.org/10.1016/j.micromeso.2013.08.029

[40] Z. Li, L. Gong, X. Cheng, S. He, C. Li, and H. Zhang, “Flexible silica aerogel composites strengthened with aramid fi bers and their thermal behavior,” *JMADE*, vol. 99, pp. 349–355, 2016, [Online]. Available: http://dx.doi.org/10.1016/j.matdes.2016.03.063

[41] T. Zhou, X. Cheng, Y. Pan, C. Li, L. Gong, and H. Zhang, “Mechanical performance and thermal stability of glass fiber reinforced silica aerogel composites based on co-precursor method by freeze drying,” *Appl Surf Sci*, vol. 437, pp. 321–328, 2018, doi: 10.1016/j.apsusc.2017.12.146.

[42] A. J. Gayle *et al.*, “Tunable Atomic Layer Deposition into Ultra-High-Aspect-Ratio (>60000:1) Aerogel Monoliths Enabled by Transport Modeling,” *Chemistry of Materials*, no. 33, pp. 5572–5583, 2021.

[43] C. Mandal, S. Donthula, P. M. Rewatkar, C. Sotiriou-Leventis, and N. Leventis, “Experimental deconvolution of depressurization from capillary shrinkage during drying of silica wet-gels with SCF CO2 why aerogels shrink?,” *J Solgel Sci Technol*, vol. 92, no. 3, pp. 662–680, Dec. 2019, doi: 10.1007/s10971-019-05124-x.

[44] E. Strobach, B. Bhatia, S. Yang, L. Zhao, and E. N. Wang, “High temperature annealing for structural optimization of silica aerogels in solar thermal applications,” *J Non Cryst Solids*, vol. 462, pp. 72–77, 2017, doi: 10.1016/j.jnoncrysol.2017.02.009.

[45] E. Strobach, B. Bhatia, S. Yang, L. Zhao, and E. N. Wang, “High temperature annealing for structural optimization of silica aerogels in solar thermal applications,” *J Non Cryst Solids*, vol. 462, pp. 72–77, Apr. 2017, doi: 10.1016/j.jnoncrysol.2017.02.009.

[46] Z. J. Berquist, A. J. Gayle, N. P. Dasgupta, and A. Lenert, “Transparent Refractory Aerogels for Efficient Spectral Control in High-Temperature Solar Power Generation,” *Adv Funct Mater*, 2021, doi: 10.1002/adfm.202108774.

[47] Z. P. Yang, L. Ci, J. A. Bur, S. Y. Lin, and P. M. Ajayan, “Experimental observation of an extremely dark material made by a low-density nanotube array,” *Nano Lett*, vol. 8, no. 2, pp. 446–451, 2008.

[48] A. Lenert *et al.*, “A nanophotonic solar thermophotovoltaic device,” *Nat Nanotechnol*, vol. 10, no. 6, pp. 563–563, 2015, [Online]. Available: http://www.nature.com/doifinder/10.1038/nnano.2015.117

[49] H. Lin *et al.*, “A 90-nm-thick graphene metamaterial for strong and extremely broadband absorption of unpolarized light,” *Nat Photonics*, vol. 13, no. 4, pp. 270–276, 2019, [Online]. Available: http://dx.doi.org/10.1038/s41566-019-0389-3

[50] V. Rinnerbauer, Y. X. Yeng, J. J. Senkevich, J. D. Joannopoulos, M. Soljačić, and I. Celanovic, “Large area selective emitters/absorbers based on 2D tantalum photonic crystals for high-temperature energy applications,” *Photonic and Phononic Properties of Engineered Nanostructures III*, vol. 8632, no. May, p. 863207, 2013, doi: 10.1117/12.2005202.

[51] H. Wang, H. Alshehri, H. Su, and L. Wang, “Design, fabrication and optical characterizations of large-area lithography-free ultrathin multilayer selective solar coatings with excellent thermal stability in air,” *Solar Energy Materials and Solar Cells*, vol. 174, no. June 2017, pp. 445–452, 2018.

[52] Z. J. Berquist, K. K. Turaczy, and A. Lenert, “Plasmon-enhanced greenhouse selectivity for high-temperature solar thermal energy conversion,” *ACS Nano*, vol. 14, no. 10, pp. 12605–12613, 2020.

Supporting Information

Large area transparent refractory aerogels with high solar thermal performance

Zachary J. Berquist,[†]
Andrew J. Gayle,[§]
Andrés Miranda Mañón[†]
Victor Vogt[#]
Keyi Kang Yao[◊]
Vishnu Ramasawmy[◊]
Kyle Wilke[◊]
Neil P. Dasgupta,[§#]*
Andrej Lenert[†]*

[†]Department of Chemical Engineering, University of Michigan, Ann Arbor, MI 48109
[§]Department of Mechanical Engineering, University of Michigan, Ann Arbor, MI 48109
[#]Department of Materials Science and Engineering, University of Michigan, Ann Arbor, MI 48109
◊AeroShield Materials, Hyde Park, MA, 02136
*E-mails: ndasgupt@umich.edu; alenert@umich.edu

Supplementary Note #1: CPD System Process Details

Fig. S1 shows typical target temperature and pressure profiles of a critical point drying run. The aerogels are loaded into the CPD at room temperature and pressure. The CPD system is sealed and purged of air by pressurizing CO_2 to 50 psi and then venting to atmospheric pressure three times. Note that the system is not filled with excess methanol, i.e., the methanol in the aerogel tiles is the only methanol in the system and the rest of the space is filled with gas before pressurization. The system is then pressurized to 1500 psi with CO_2 pumped from dewars into the vessel through the lid over the course of 3 h, keeping pressurization rate less than 10 psi/min, while maintaining room temperature. The CO_2 entering the vessel is first passed through a heat exchanger to set the inlet temperature. Due to the relatively large volume of the CPD vessel compared to the total aerogel tile volume in the vessel, the methanol content in the vessel after pressurization is complete is typically less than 10 %. Once at pressure, CO_2 is continuously pumped into the system while maintaining pressure at 1500 psi by venting the system from the side opposite the CO_2 inlet. During this CO_2 exchange, CO_2 is provided at a rate of approximately $\frac{Volume_{CPD}\,[Liters]}{Pump\ Rate\ CO_2\ [\frac{Liters}{h}]} \approx 2\ h$ in order to fully displace the vessel volume every two hours. During this exchange, a recirculating heater provides hot water to the CPD vessel jacket to raise the internal temperature of the system to 50°C at a rate of approximately 0.15 °C/min. The CO_2 exchange continues until the methanol content in the CPD falls below 0.5 % methanol, which is monitored via the system vent. This typically requires four full displacements of the vessel volume and requires a total of 8 h of CO_2 exchange. After the target methanol content is reached, the system is depressurized over 5 h at a rate of approximately 5 psi/min while maintaining a temperature of 50 °C. The system is not automated. Therefore, these rates are approximate and can vary by up to 10-20 % each batch. At this level of run variation, we do not observe significant variation in aerogel tile quality.

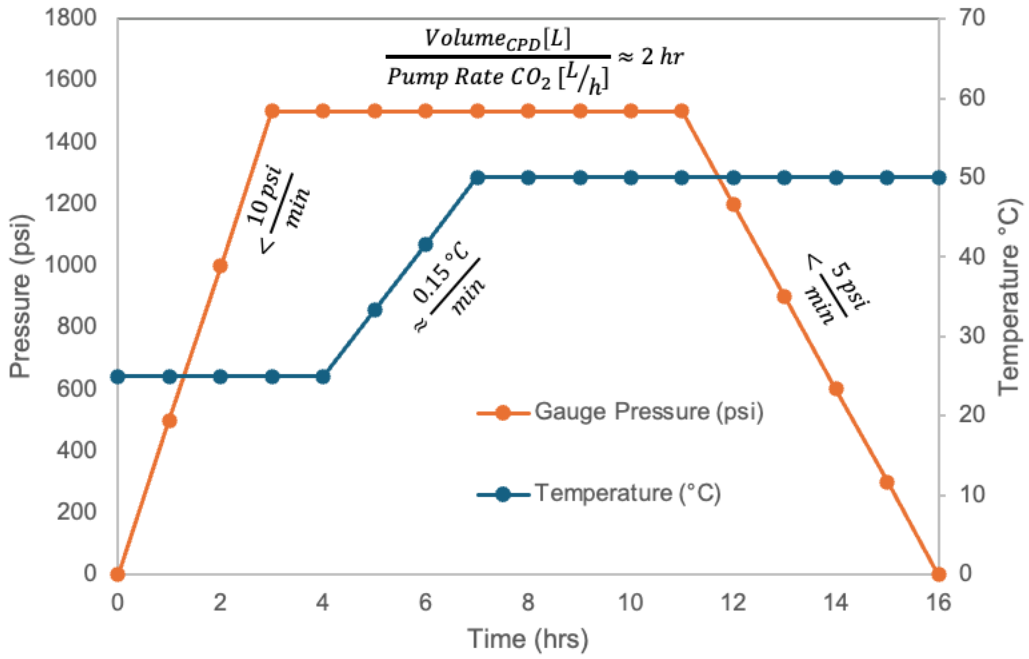

Figure S1. Typical CPD run profile consisting of pressurization, CO_2 exchange, and depressurization stages.

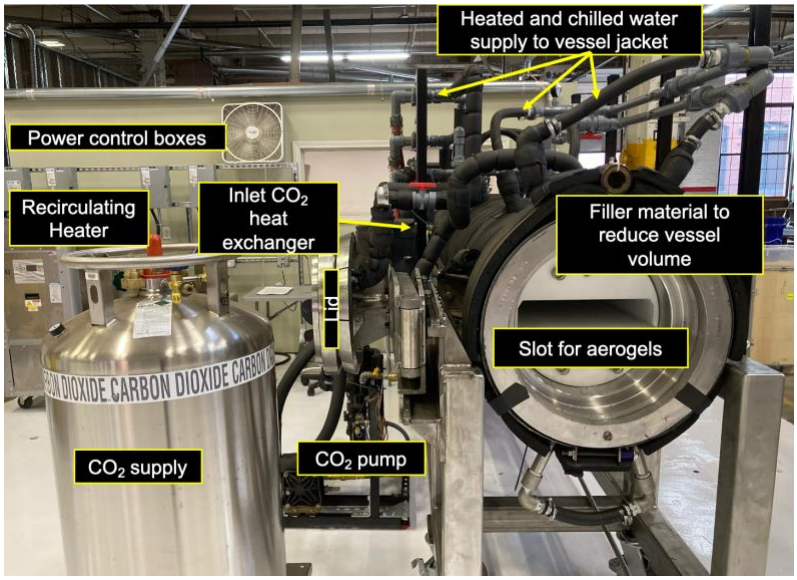

Figure S2. 500-liter CPD system used to synthesize aerogel sheets

Supplementary Note #2: ALD Model Parameters and Variables

Table S1: ALD parameters used for QSM-ALD model inputs. Relevant equations and other variables can be found in our previous publication.

Symbol	Description	Value - LD	Value - MD	Units
t	Model time step	$1*10^{-4}$		s
T	Deposition temperature	423		K
V	Volume of the chamber	$1.2*10^{-3}$		m^3
S	Precursor saturation dose (TMA)	$5.3*10^{18}$		$1/m^2$
M_A	Molar mass of TMA	72.09		g/mol
P	Initial pressure of TMA in the chamber after a pulse[i]	6.5		Torr
A_0	Projected surface area of tiles[ii]	$5.4\text{-}6.3*10^{-4}$	$4.1\text{-}4.4*10^{-4}$	m^2
SSA_{SiO2}	Specific surface area (per gram of silica)[iii]	573	529	m^2/g
d	Pore diameter[iv]	$36*10^{-9}$	$32*10^{-9}$	m
B	Initial volumetric surface area	$3.7*10^7$	$7.4*10^7$	m^2/m^3
φ	Aerogel porosity	98	95	unitless
τ	Tortuosity (fitted)	1.0[v]	2.1	unitless

[i]This was estimated by varying the exposure time and number of doses before dosing the counter reactant in the ALD chamber and evaluating the infiltration depth for HD-BM samples, which have known properties.[1] The initial TMA partial pressure at the start of each dose was fit to the infiltration depth data.

[ii]The size of each tile used for the analysis varied slightly. Details on the sample size for each condition are listed in Table S2.

[iii]See Supplementary Note #3 for the calculation of SSA_{SiO2}

[iv]N_2 sorption measurements were taken as described in our previous publication [1]. The Barrett-Joyner-Halenda (BJH) method was used to calculate pore size distributions based on the adsorption branch of the isotherm. The adsorption branch was used as opposed to the desorption branch to limit the effects of mechanical deformation of the aerogels, which is more significant in the desorption branch, on the analysis [2]. While it is known that gas sorption measurements have limitations for characterizing the structure of aerogels [2], it provides a reasonable input for fitting the transport model for ALD modification. The surface area available for ALD was calculated via mass gain, rather than using Brunauer–Emmett–Teller (BET) surface area analysis (Supplementary Note #3).

[v]While this tortuosity is likely an underestimation, it allows for a reasonable fit to the experimental data (Supplementary Note #5).

Table S2: Approximate dimensions and infiltration depths of aerogels used for each ALD condition. Infiltration depths for LD samples were measured using SEM/EDS, while MD samples were measured using optical microscopy.

Sample	**No. Doses**	**Exp. Time (s)**	**A_0 ($*10^{-4}$ m^2)**	**Infil. Depth (µm)**	**Sample**	**No. Doses**	**Exp. Time (s)**	**A_0 ($*10^{-4}$ m^2)**	**Infil. Depth (µm)**
LD-1	1	122.5	5.4	880	MD-1	1	122.5	4.4	390
LD-2	2	122.5	6.1	1130	MD-2	3	122.5	4.4	730
LD-3	3	122.5	6.3	1500	MD-3	5	122.5	4.2	950
LD-4	3	17.5	6.1	560	MD-4	5	32.5	4.1	490
LD-5	3	62.5	6.2	1020	MD-5	5	62.5	4.2	750

Supplementary Note #3: Calculation of initial specific surface area

For input into the ALD model, the surface area per gram of silica prior to ALD modification (SSA_{SiO2}) is estimated using the ALD mass gain. This is a representative measure of the surface area that is modified via ALD and is more relevant for ALD modeling purposes. Additionally, this avoids some of the potential complications involving N_2 sorption measurements and BET surface area analysis, which can introduce inaccuracies [2,3].

The initial mass of aerogel samples was measured using an analytical balance following drying under vacuum for at least 1 h at 150 °C to remove adsorbed water. After removal from the ALD chamber, the measurement was performed 1-2 min to limit water adsorption. The ALD-modified aerogel mass was measured similarly. Mass gain measurements were performed using fully modified samples.

Table S3. Aerogel mass gain measurements for large aerogel tiles. In both cases the mass gain percentages were consistent to within ±1.0% for each sample.

Sample Type and Number	Average Mass Gain (%)	Number of Samples
LD	26.2	2
MD	24.2	13

SSA_{SiO2} was calculated using Equation S1 [1]:

$$SSA_{SiO2} = \frac{MG(\%)}{GPC * (1\ cycle) * \rho_{Al2O3} * 100\%} \quad \text{(S1)}$$

where MG(%) is the percentage mass gain, GPC is the growth per cycle on planar SiO_2 [1.4 Å/cycle], and ρ_{Al2O3} is the bulk density of ALD Al_2O_3 [3.24 g/cm^3]. Measurement details and more in-depth discussion can be found in our previous publication [1]. The calculated values for SSA_{SiO2} for both LD and MD samples can be found in Supplementary Note #2.

Supplementary Note #4: Estimating infiltration depth using optical microscopy

The infiltration depth can be estimated using optical microscopy by evaluating the location where an interface is visible, which is possibly due to a change in the refractive index of the aerogel in the ALD-modified region (Fig. S2c). Evaluating the infiltration depth optically has the benefit of being non-destructive and faster measurement time. To evaluate the accuracy of evaluating the ALD infiltration depth using optical microscopy, compared to elemental linescans collected via SEM/EDS, the infiltration depth was evaluated in multiple positions in a sample. Table S4 shows the evaluated infiltration depths for SEM/EDS and optical microscopy for a single sample, while Fig. S2 shows an example of each measurement. As shown in Table S4, the infiltration depths as measured by the two techniques are similar.

Table S4. Infiltration depth measurements using SEM/EDS and optical microscopy. The sample surface column indicates which side of the aerogel tile is evaluated.

Sample Surface	Technique	Number of Measurements	Mean and Standard Deviation of Infiltration Depth (mm)
Bottom	SEM/EDS	4	1.78 ± 0.04
	Optical Microscopy	11	1.80 ± 0.02
Top	SEM/EDS	4	1.53 ± 0.03
	Optical Microscopy	11	1.54 ± 0.01

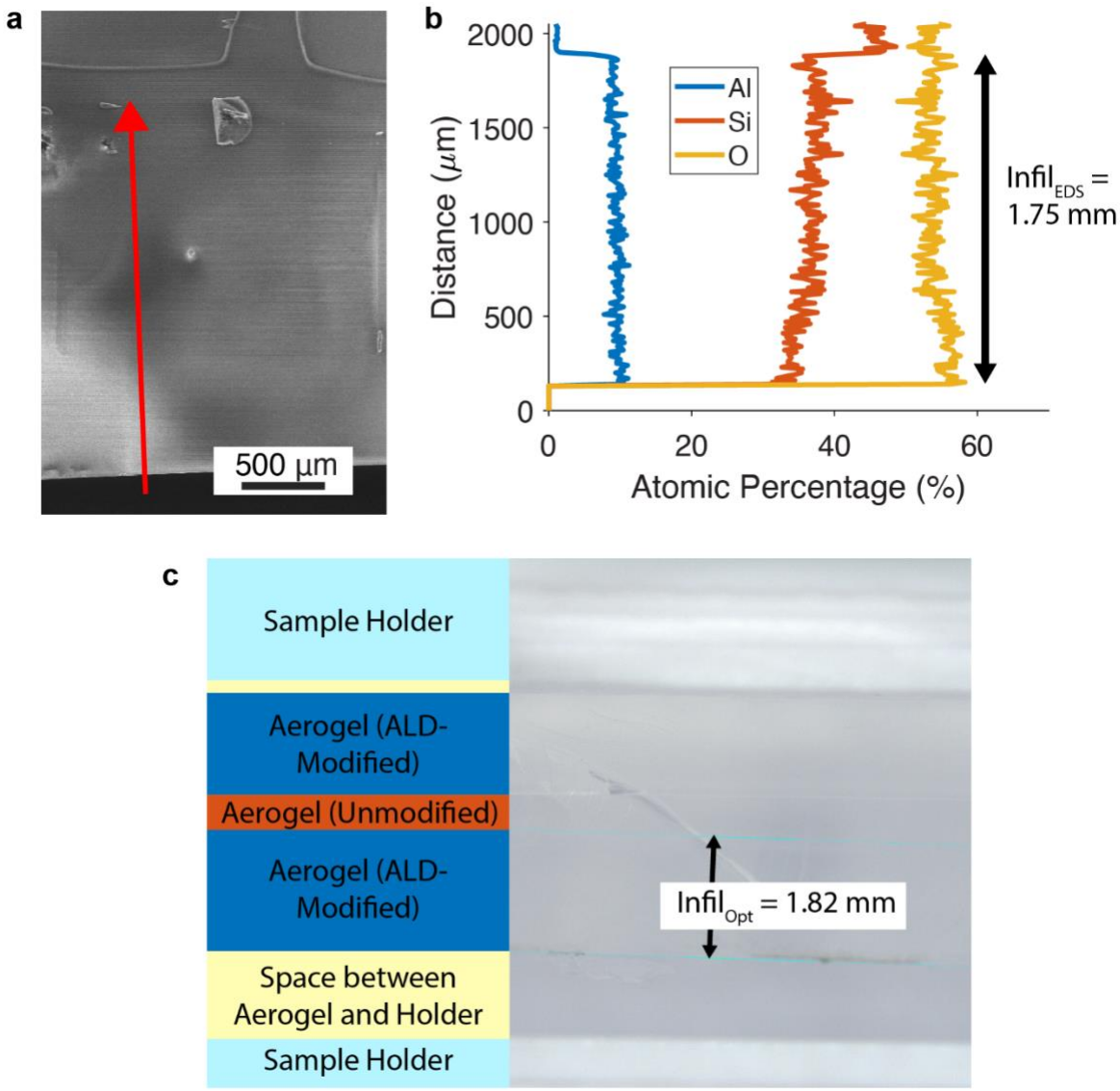

Figure S2. Infiltration depth as evaluated using SEM/EDS and optical microscopy. (a) Example SEM image of the cross-section of the edge of an aerogel tile. The arrow shows the location of the EDS linescan in (b). **(b)** EDS linescan showing the percentage of Al, Si, and O through the aerogel cross-section. **(c)** Optical microscopy image demonstrating the change in contrast in the ALD-modified region, and the resulting measurement of infiltration depth.

Supplementary Note #5: QSM-ALD model results for LD aerogels

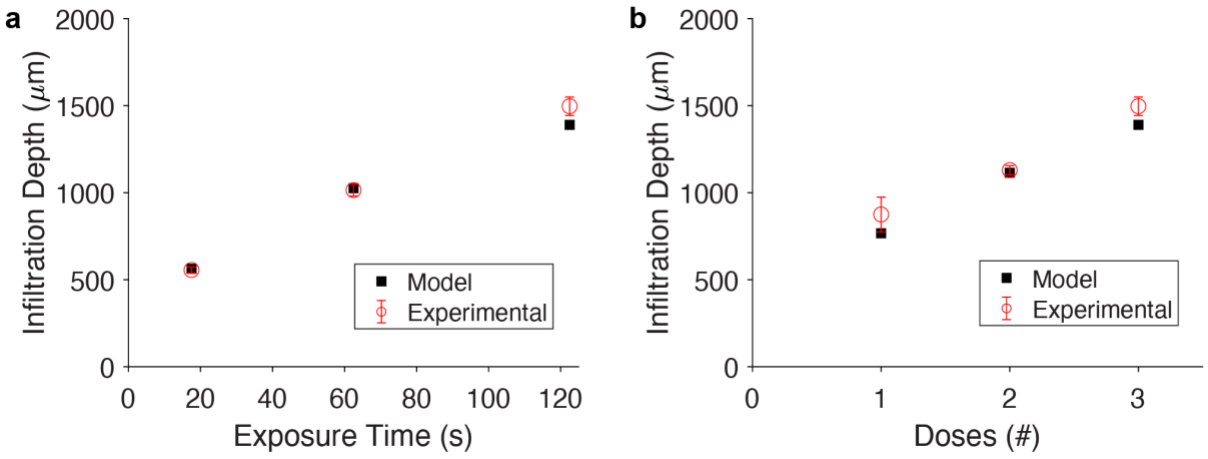

Figure S3. Experimental and modeling results for LD aerogels. The parameters used for modeling are shown in Supplementary Note #2. The error bars are representative of the standard deviation from 3-6 measurements in each case. (a) Variation in exposure time per dose while keeping the number of doses constant, and (b) variation in number of doses while keeping exposure time constant.

The experimental and modeling results for LD aerogels are shown in Fig. S3. The underestimated value for the fitted tortuosity (1.0) is likely due to slight inaccuracies in the N_2 sorption results, which is known to lead to somewhat erroneous results when insufficient time is given for equilibration. Additionally, the BJH method, commonly used to determine pore sizes, is known to underestimate aerogel pore volume in some circumstances due to macropores not being included in the BJH analysis or lack of N_2 condensation in the pores. Other possible reasons for this discrepancy include inaccuracies in the surface area (which is calculated using the mass gain, see Supplementary Note #3), inaccuracies in the experimentally measured infiltration depth, or simplifications associated with the model assumptions [1]. Investigating these possible reasons will be performed in a future study. Regardless of the origin, the modeled data reasonably captures the trends in the infiltration depth.

Supplementary Note #6: Process parameters for ALD modification of scaled-up aerogel tiles

The precursor flow is controlled by a pneumatic valve (C_v = 0.27), which is pulsed for a fixed length of time while the chamber is held under passive vacuum. The pulse times were selected for each reactant based on a set of experiments to determine the pulse time at which the amount of precursor dosed reached a plateau. The carrier gas flow rate is set by a mass flow controller (MFC).

Temperature is controlled by a PID controller monitoring temperature at the base of the chamber and on the chamber lid, as well as at the inlets and outlets of the reactor. The chamber is held at 150 °C during the course of the process, and the inlet and outlets are held at 140 °C.

The reaction chamber uses a cross-flow design and growth uniformity of the ALD process was validated to be within 5 % on silicon wafers. During the aerogel reaction process, the chamber is isolated with pneumatic valves at the manifold inlet and reactor outlet and held under passive vacuum. In our previous work, it was shown that the Knudsen diffusion coefficient within the aerogel pores is much smaller than the bulk diffusion coefficient in the ALD reactor, which suggests that the precursor partial pressure in the chamber is relatively uniform relative to the precursor partial pressure profile within the pores [1].

Table S5: Process parameters and modeled results (infiltration depth, percentage of unreacted precursor, and total process time) for an example sample from each sample type. Details on the multidose-QSM-ALD method can be found in our previous publication [1]. Three deposition conditions are shown for each sample for comparison. The deposition conditions with a * indicate the recipe that was implemented. A_0 in each case was 150 x 70 mm.

Sample Type	Deposition Conditions[i]	Predicted Infiltration Depth (mm)	Unreacted Precursor (%)[ii]	Process Time (h)[iii]
LD*	20 doses, 30 s exp. + 20 doses, 60 s exp. + 28 doses, 120 s exp.	2.8	1	12
LD	86 doses, 30 s exp.	2.8	9	8
LD	68 doses, 120 s exp.	2.8	1	17
MD*	50 doses, 30 s exp. + 50 doses, 60 s exp. + 59 doses, 120 s exp.	2.7	7	23
MD	260 doses, 30 s exp.	2.7	19	16
MD	143 doses, 120 s exp.	2.7	3	32

[i]For deposition conditions with variable exposure times, the exposure time was increased when the modeled percentage of unreacted precursor for an individual dose increased beyond ~2.5% (LD samples) or ~12.5% (MD samples).

[ii]This assumes that the aerogel is twice the thickness of the predicted infiltration depth, i.e. the aerogel is not fully modified until the last dose. In reality, there is some overshoot in the infiltration depth to ensure complete modification. This was necessary due to variations in sample thickness, which were difficult to measure and account for due to the fragility of the aerogels.

[iii]The purge time is double the exposure time, and the same number of doses and purging procedure were used for the DI water doses as the TMA doses. Additionally, this includes a 2 h wait time before starting any doses, as well as the 50 initial DI water doses (details in Experimental Section).

Supplementary Note #7: Density and porosity changes at high temperatures

Using the shrinkage data from Fig. 4a in the main text, the density and the porosity of the aerogels during the aging process are estimated. ALD increases the density of the aerogels by ~25 % due to the increase in mass. After aging for just 2 – 4 days at 700 °C, however, the density of the unmodified aerogels exceeds that of the refractory aerogels because of their higher densification rate. A similar trend holds for the porosity (Fig. S4b).

Alumina-coated aerogels exhibit enhanced resistance to high-temperature structural changes. BET measurements have shown a larger specific surface area and higher porosity following intensive heat treatments compared to pure silica aerogels [4]. UV-Vis-NIR and FTIR analyses showed a minimal increase in light scattering after aging, indicating suppression of particle and pore growth. These effects were attributed due to the modified surface chemistry consisting of Al-O-Si moieties, as confirmed through XPS.

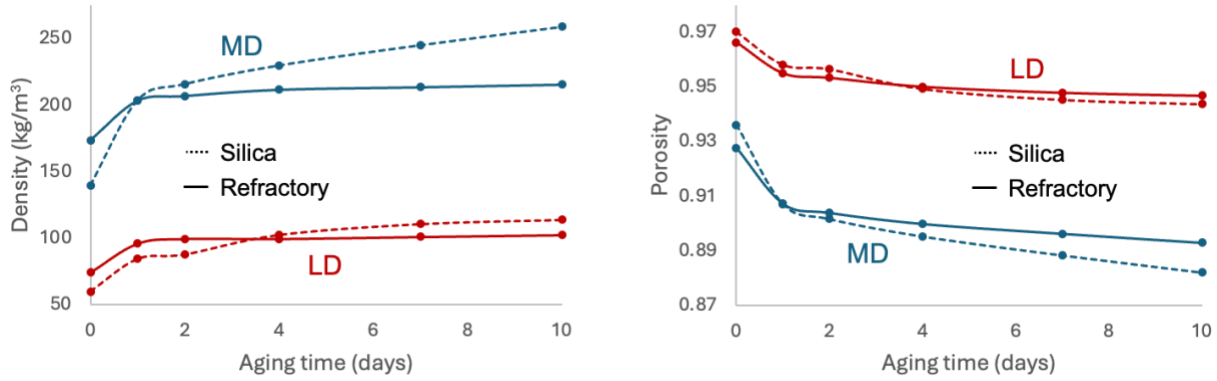

Figure S4. Aerogel density (a) and porosity changes (b) at 700 °C. The unmodified silica aerogels are initially lower density (higher porosity) but become higher density (lower porosity) than their ALD-modified counterparts (higher lines).

Supplementary Note #8: Temperature and irradiance dependent FOM

Our previous work details a simplification of the figure-of-merit which we summarize here. Equation 1 from the main text (reprinted below) can be reduced to Equation S2:

$$\eta = \alpha_{abs}\tau_{glass}\tau_{aerogel} - \frac{\varepsilon_{app}\sigma T^4}{H_s} \quad (1)$$

$$\eta = \alpha_{abs}\tau_{glass}\tau_{aerogel} - \varepsilon_{app}\Phi \quad (S2)$$

where Φ is the relative temperature. Φ is defined as:

$$\Phi = \frac{\sigma T^4}{H_s} = \frac{\sigma T^4}{Q_{sol}C} \quad (S3)$$

Equation S3 highlights a useful relationship. The scaling associated with a lower concentration ratio is effectively the same as increasing the operating temperature of the receiver. Either change increases the relative amount of thermal losses compared to incoming sunlight.

Fig. S5 shows how the absorber temperature affects the slope of the efficiency lines. At higher solar irradiance, H_s, it is easier to achieve a higher figure-of-merit, so the minimum material properties are lower. Alternatively, better aerogel properties are needed at lower irradiance. Linear concentrators have a wide range of concentration ratios from 30 to 100. If we assume an irradiance of 75 Suns, η at 700 °C increases to 73 %. Alternatively, η drops to 50 % at 35 Suns. Fig. S5 reveals another important aspect of solar receiver design. The figure-of-merit cannot exceed the transmittance of an aerogel (or solar absorptance of a SA) even if there is perfect thermal resistance. Since our aerogels are very transparent (~96 %), they have broad appeal in CST since they can operate efficiently at high irradiances and lower temperatures, which is illustrated by the decreasing slope of the contour lines in Fig. S5. In solar power towers, for example, aerogels may decrease the number of heliostats required while maintaining conversion efficiency.

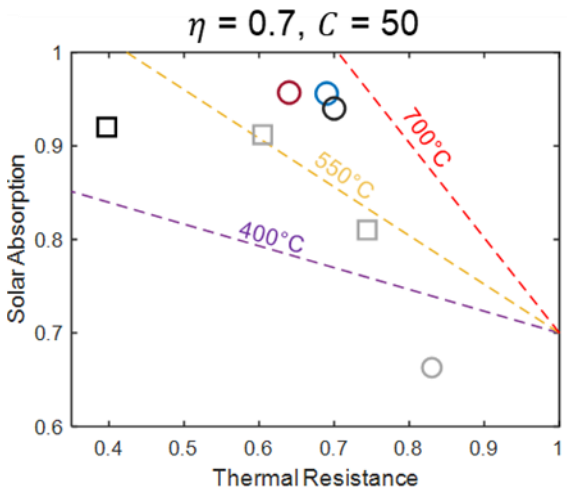

Figure S5. Contours of 70 % efficiency at varying temperatures. The lower the temperature (or higher the concentration ratio), the smaller the slope of the efficiency contour. Either lowering the temperature or increasing the concentration lowers the relative temperature, having a similar impact on receiver performance.

Supplementary Note #9: Extended heat treatment of aerogel tiles

Fig. S6 shows the decreasing length of aerogel monoliths over a 20-day heat treatment. The study includes a pre-treatment for 2 days at 800 °C and a heat treatment at 700 °C for the remaining 18 days. These samples are not from the same batch as the those discussed in the main text but exhibit a similar post-ALD density of 140 kg/m^3.

These data show a similar linear shrinkage rate as the MD refractory aerogels of 0.098 % per day (Table 1). If this shrinkage rate is assumed to remain constant, the aerogel tiles would shrink to 80% of their installed length after ~5,000 h of continuous operation at 700 °C. This period corresponds to approximately 1.7 years, assuming the solar receiver operates 8 hours a day. After this period, the aerogel receiver would likely require maintenance to close the gaps between neighboring aerogel tiles caused by the shrinkage (the receiver performance is assumed to be proportional to the receiver area covered by the aerogel tiles).

It is important to note that this lifetime estimate is a lower bound. Strobach *et al*. conducted a long-term annealing study on aerogels at elevated temperatures and showed that the densification rate of silica aerogels at 600 °C after 50-100 days is an order of magnitude lower than during the first 10-20 days [5]. We similarly expect the shrinkage rate of refractory aerogels at 700 °C to slow down and result in an order of magnitude longer lifetime than the conservative estimate described above.

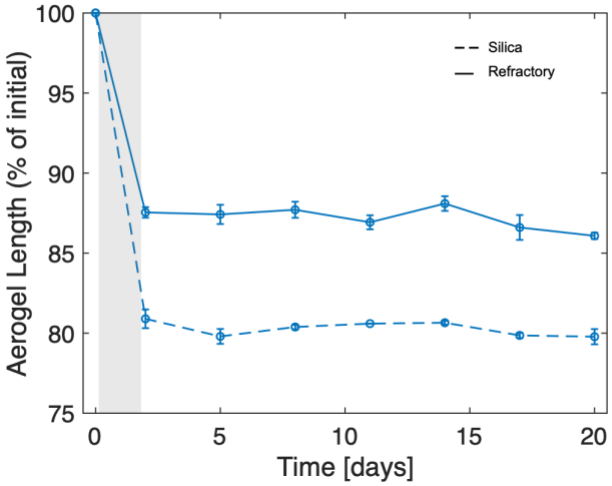

Figure S6. Length change of aerogel tiles over a 2-day pre-treatment at 800 °C (in air) and an 18-day period at 700 °C (in air). The shaded area highlights the period of the pre-treatment at a higher temperature. Medium density (MD) aerogels with an ALD coating (solid) and without (dashed).

Supplementary Note #10: Optical Property Measurements of Aerogels

Transmittance of the aerogels was measured with a UV-Vis-NIR and FTIR spectrophotometers. Aged silica and refractory aerogels have similar solar-weighted transmittances. Refractory aerogels have increased water absorption in the infrared due to the aluminum sites.

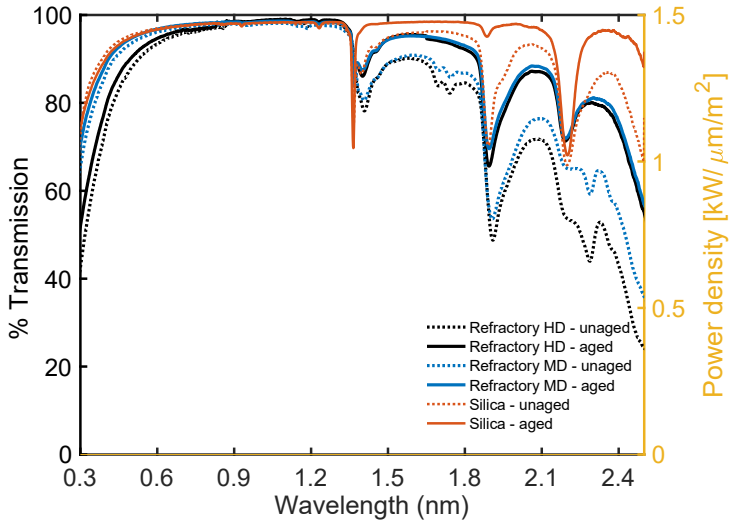

Figure S7. Hemispherical transmittance of the coated (refractory) and uncoated (silica) aerogels obtained using a UV-Vis-NIR equipped with an integrating sphere. The AM1.5D spectrum is shown for reference. High density (HD); medium density (MD).

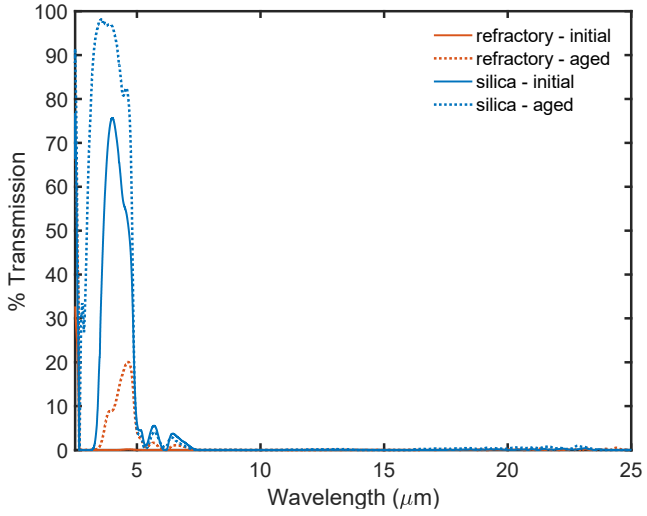

Figure S8. Hemispherical transmittance of the coated (refractory) aerogels and uncoated (silica) samples obtained using a FTIR spectrophotometer. Data shown for medium density (MD).

References

[1] A. J. Gayle *et al.*, "Tunable Atomic Layer Deposition into Ultra-High-Aspect-Ratio (>60000:1) Aerogel Monoliths Enabled by Transport Modeling," *Chemistry of Materials*, no. 33, pp. 5572–5583, 2021.

[2] M. Aegerter, N. Leventis, and M. Koebel, "Aerogels handbook (Advances in Sol-Gel Derived Materials and Technologies)," in *Springer*, 2011, p. 932.

[3] B. C. Dunn *et al.*, "Silica aerogel supported catalysts for Fischer-Tropsch synthesis," *Appl Catal A Gen*, vol. 278, no. 2, pp. 233–238, Jan. 2005, doi: 10.1016/j.apcata.2004.10.002.

[4] Z. J. Berquist, A. J. Gayle, N. P. Dasgupta, and A. Lenert, "Transparent Refractory Aerogels for Efficient Spectral Control in High-Temperature Solar Power Generation," *Adv Funct Mater*, 2021, doi: 10.1002/adfm.202108774.

[5] E. Strobach, B. Bhatia, S. Yang, L. Zhao, and E. N. Wang, "High temperature stability of transparent silica aerogels for solar thermal applications," *APL Mater*, vol. 7, no. 8, Aug. 2019, doi: 10.1063/1.5109433.